A new scenario for ‹c› vacancy loop formation in zirconium based on atomic-scale modeling

B. Christiaen, C. Domain, L. Thuinet, A. Ambard, A. Legris

To cite this version:

B. Christiaen, C. Domain, L. Thuinet, A. Ambard, A. Legris. A new scenario for ‹c› vacancy loop formation in zirconium based on atomic-scale modeling. Acta Materialia, 2019, 179, pp.93-106. ⟨10.1016/j.actamat.2019.07.030⟩. ⟨hal-02445245⟩

HAL Id: hal-02445245

https://hal.science/hal-02445245v1

Submitted on 20 Jul 2022

Version of Record: https://www.sciencedirect.com/science/article/pii/S1359645419304707
Manuscript_74a62704b3acd880111a874458712baf

A new scenario for ‹c› vacancy loop formation in zirconium based on atomic-scale modeling

B. Christiaen [a,b,c], C. Domain [a,c], L. Thuinet [b,c], A. Ambard [a,c], A. Legris [b,c]

[a] EDF-R&D, Département Matériaux et Mécanique des Composants (MMC), Les Renardières, F-77818 Moret sur Loing Cedex, France

[b] Univ.Lille, CNRS,INRA, ENSCL, UMR 8207,UMET, Unité Matériaux et Transformations, F 59 000 Lille, France

[c] Laboratoire commun EDF-CNRS Etude et Modélisation des Microstructures pour le Vieillissement des Matériaux (EM2VM), France

Keyword:

Zirconium, dislocation loop, DFT, elasticity, stacking fault pyramids

Abstract

The growth of zirconium alloys under irradiation is a phenomenon experimentally identified and associated with the development beyond a threshold dose of dislocation loops with vacancy character having a Burgers vector with a component parallel to the c axis. In this work, by combining atomic simulations (DFT and empirical potential) and continuous modeling, we show that prismatic stacking fault pyramids or bipyramids whose base rests on the basal plane of the hcp structure are likely precursors to the formation of c vacancy loops. In other words, these would not be formed by progressive accretion of vacancies but rather by collapse of the pyramids or bipyramids beyond a certain size. This mechanism could explain the fact that the ‹c› vacancy loops are never observed below a size of the order of 10 nm and their appearance at high fluence.

I. Introduction

Zirconium alloys are used as fuel cladding or as guide tube in fuel assembly of Light Water Reactor (LWR). In the core, neutron irradiation generates a large number of vacancies and self-interstitials (SIAs) which cluster in dislocation loops. Zirconium-made components change their dimensions under irradiation. Unlike steels or nickel-based alloys, they do not swell and the dimensional change called growth is essentially volume conservative though a small volume increase has been observed under particular experimental conditions [1]. Experimental observations show that above a threshold dose those alloys are prone to an accelerated growth called “breakaway” [2]. It is well established that two types of dislocation loops ‹a› and ‹c› which differ by their Burgers vector are directly responsible for the growth of zirconium alloys under irradiation. In particular, ‹c› loops appearance is correlated with breakaway [3] (see [4] and [5] for review).

Many authors have studied defect clusters in post-irradiation microstructure of zirconium alloys by using transmission electron microscopy (TEM), a compilation of observations being given by Griffiths [5]. For neutron-irradiated zirconium alloys for low irradiation dose ($< 5\times10^{25}$ nm^{-2}) at temperatures between 250 and 400°C, numerous studies [2–13] reveal a high density (typically between 5×10^{21} and 5×10^{22} m^{-3}) of perfect dislocation loops of vacancy or interstitial nature with Burgers vector $\frac{1}{3}\langle 11\bar{2}0\rangle$ (‹a›-type) of diameter between 5 and 20 nm. The three ‹a› Burgers vectors are equally represented and the proportion of ‹a› vacancy loops increases with the irradiation temperature [5,9]. The loop habit plane is close to the first-order prismatic plane $\{10\bar{1}0\}$ but the ‹a› loops are not pure edge and are aligned in rows parallel to the basal plane (‘corduroy contrast’) [5,6]. Increasing the irradiation temperature T induces a decrease in the loop density ρ and an increase of the loop size $\bar{d}$ [9] (for a neutron-irradiated Zy-2 up to a fluence of 1×10^{25} nm^{-2}, 8 nm $< \bar{d} <$ 10 nm and $8\times10^{21} < \rho < 5\times10^{22}$ m^{-3} at T = 350 °C whereas 16 nm $< \bar{d} <$ 23 nm and $4\times10^{21} < \rho < 2\times10^{22}$ m^{-3} at T = 400 °C). For fluence higher than 5×10^{25} nm^{-2}, existence of ‹c› component loops was evidenced [3,5,8,14–16]: they are usually faulted, of the vacancy type and located in the basal plane with a Burgers vector $\frac{1}{6}\langle 20\bar{2}3\rangle$ having a component parallel to the ‹c› axis. Loops with a Burgers vector $\frac{1}{2}[0001]$ have also been identified [7]. The ‹c› component loops are much larger than the ‹a› loops, their lowest observed diameter is around 10 nm [11] but their density is much lower. Whatever the irradiation conditions, there is coexistence of these ‹c› component loops with more numerous and smaller ‹a› loops. In order to observe these ‹c› loops by TEM, the g=0002 diffraction vector is used to make ‹a› loops invisible. From all the obtained data, it turns out that zirconium is extremely resistant to void formation during neutron irradiation [5,17] which may be due to the fact that vacancy type loops are easily formed.

Cluster Dynamics (CD) methods [12,18] or the Production Bias Model (PBM) [19] were used to model microstructure evolution and the resultant growth of zirconium alloys under irradiation. Christien et al. [18] developed a CD model assuming a diffusion anisotropy difference (DAD) [20] between vacancies and SIAs. They also hypothesized that ‹c› dislocation loops nucleate on small iron clusters. Indeed, the experimental results of De Carlan et al. [21] show a greater ‹c›-loop density close to the intermetallic precipitates $Zr(Cr,Fe)_2$. However, the nucleation rate of ‹c› dislocation loops was arbitrarily fixed. In the case of the PBM, Barashev et al. [19] used ‹a› and ‹c›-loop densities as fitting parameters. On the whole, in each of these approaches, the nucleation of ‹c› loops was adjusted to numerically reproduce the experimental results, whereas a physical and detailed description of the mechanism leading to their formation is still missing.

In order to improve the knowledge of these microstructural defects, atomic-scale simulations were performed. Kulikov et al. [22] modelled ‹c› dislocation loops using a tight-binding potential based on Zr properties at equilibrium. Their results showed that loops with extrinsic and intrinsic I_1 basal fault can be stabilized. Varvenne et al. [23] also simulated these two types of loop using Mendelev and Ackland potential [24] and calculated their formation energies. They used a line tension model [25] to extrapolate their data to larger loop diameters and showed that the formation of ‹a› dislocation loops was energetically favorable.

Voskoboinikov et al. [26] simulated displacement cascades by molecular dynamics (MD) in zirconium to identify residual defects using a short-range manybody potential [27]. They identified various configurations of vacancy clusters among which stacking fault pyramids with six faulted interfaces in the pyramidal planes and an extrinsic fault on the basal plane but no ‹c› loop. Di [28] also observed these pyramids in the displacements cascades obtained with the EAM potential developed by Mendelev and Ackland [24], but with an intrinsic basal fault.

The goal of this paper is to determine if the pyramids formed in displacements cascades can play the role of precursor for the formation of ‹c› loops. For this purpose, we used various atomistic simulation methods such as Density Functional Theory (DFT) and empirical potential EAM (Embedded Atom Method) detailed in section II to explore the mechanisms of ‹c›-loop formation. By using the EAM potential, the simulation results revealed that a perfect ‹c› loop can be generated from the collapse of a bipyramid, as shown in section III, but such a transition cannot be evidenced in DFT calculations due to the size of the defects for which this transition may occur. As a consequence, DFT data were used to parameterize mesoscopic laws describing the formation energy of loops and pyramids. These mesoscopic laws are established in section IV and allowed to investigate the relative stability of these defects at larger sizes. The results are discussed in section V.

II. Methods

The *ab initio* calculations presented in this paper are based on the density functional theory (DFT) implemented within the VASP code (Vienna *Ab initio* Simulation Package) [29] and are performed in GGA (Generalized Gradient Approximation) with PW91 (Perdew Wang 91) exchange-correlation functional [30]. The density functional or Kohn-Sham equations are solved with projector-augmented-wave (PAW) potentials [31] including 4 electrons in the valence band. The plane-wave cutoff energy in the expansion of the wave functions is set to 270 eV. The integration of the Brillouin zone is performed with Methfessel-Paxton smearing scheme [32] with a smearing value of 0.2 eV. The size of the supercell depends on the size of the defect cluster and is up to 15×15×11 unit cells containing 4950 atoms. The k-point grids are 1×1×1 in case of large supercells which contain more than 800 atoms (cf. Table 1). Calculations are performed at constant volume with lattice parameters a = 3.23 Å and c = 5.59 Å. The energies are corrected with the ANETO program [33] in order to remove the elastic interactions of the defect with its periodic images.

Table 1: Size of the supercells (x × y × z hexagonal primitive cells composed of 2 Zr atoms) as well as the associated k-point grids.

Supercell	4×4×3	5×5×4	9×9×5	12×12×8	15×15×8	15×15×8
Number of atoms	96	200	810	2304	3600	4950
k-points	4×4×4	3×3×3	2×2×2	1×1×1	1×1×1	1×1×1

The EAM potential # 3 developed by Mendelev and Ackland [24] is used in Molecular Statics (MS) calculations since it reproduces reasonably well the bulk properties, such as the elastic constant and some other small-scale quantities such as the prismatic and basal fault energies. All the MS calculations are performed with the LAMMPS code (Large-scale Atomic Molecular Massively Parallel Simulator [34]) and the conjugate gradient algorithm is used to minimize the system energy. Like in the DFT calculations, the size of the supercell depends on the size of the defect. The largest simulation defect contains 40 000 vacancies embedded in 300×300×300 unit cells (54 million atoms).

With these methods, it is possible to determine different quantities of interest such as the formation energy and the eigenstrain of a defect [35]. The calculation of these properties is detailed in Appendix A and Appendix B.

III. Characterization of the calculated defects

‹c› perfect dislocation loops and stacking fault bipyramids

In order to build perfect ‹c› loops of Burgers vector $\vec{b} = [0001]$, two atomic layers A and B of hexagonal form, each containing the same number of atoms (cf. Figure 1-a), were removed from the perfect crystal. This initial configuration was then relaxed by DFT and EAM calculations.

An unexpected result was first obtained in DFT: instead of conserving a perfect ‹c› loop structure, the initial configuration evolved towards a hexagonal bipyramid with stacking faults along the first order pyramidal planes (cf. Figure 1-b) and no stacking fault in the basal plane. An example of such an evolution is represented in Figure 1 for a defect containing 96 vacancies. This specific pyramidal structure results from the collapse of the atoms above and below the removed atomic layers to fill this empty space. This type of evolution was observed in the whole range of defect sizes simulated in DFT (up to 138 vacancies).

MS calculations also showed a similar collapse of the atoms with the formation of the same type of bipyramids around the initial loop. However, at larger defect sizes not investigated in DFT, MS calculations revealed that the bipyramid shape changes. The stacking fault along the pyramidal plane gradually disappears as the defect size increases and an almost perfect basal loop is obtained for around 40 000 vacancies in the defect (cf. Figure 2). The transition from the bipyramid to the perfect loop starts for an initial loop diameter of 20 nm, corresponding to 5 000 vacancies. Then, MS simulations show that a critical size of the defect has to be reached in order to observe this transition. These MS results allow to interpret those obtained in DFT: the largest defect cluster simulated in DFT contains 138 vacancies, a number probably below the critical size, which explains why bipyramids are stabilized in DFT instead of perfect loops.

This progressive transition exhibited in MS calculations is an interesting result because it suggests an original mechanism, in which stacking fault bipyramids could play the role of precursor for the formation of ‹c› loops, a scenario which has never been proposed before to describe dislocation nucleation in zirconium. However, due to the limited precision of the EAM potential used in MS, it would be necessary to establish if the same conclusions hold in DFT to confirm such a scenario. Unfortunately, according to the MS results, it would be necessary to perform DFT calculations with millions of atoms in the simulation box which is unreachable nowadays. Then, an alternative approach already used in [23] would consist in using physically-based mesoscopic laws to describe the formation energies of loops and pyramids adjusted on DFT calculations. Comparing the formation energies of these different objects should allow to conclude on their relative stabilities. In this procedure, it is then required (i) to establish these mesoscopic laws, which is done in section IV, and (ii) to collect the DFT data on which the mesoscopic laws are adjusted, which is the purpose of this section. Since the transition shown in Figure 2 exhibits the peculiar role of bipyramids and perfect loops, all the results concerning their formation energies as a function of the number of vacancies are represented in Figures 5 and 6. In the case of bipyramids, the MS values are higher than the DFT ones whatever the size of the defect. For perfect loops, only MS results are reported in Figures 5 and 6 since these objects could not be stabilized in DFT calculations.

Even if some perfect loops were experimentally observed in zirconium, the majority of ‹c› loops are faulted with a Burgers vector $\vec{b} = 1/6\langle 20\bar{2}3\rangle$. It would then be interesting to determine if faulted ‹c› loops could also be formed from 3-dimensional defects such as pyramids. In order to investigate this scenario, it is required to calculate the formation energies of these objects, which is the aim of the following part.

Stacking fault pyramids and ‹c› faulted loops I_1

In order to build these objects, the first step is to remove a hexagonal atomic layer in the basal plane of the hcp structure. The atoms constituting the pyramid are then selected beforehand (they are those atoms inside the object delimited by the prismatic planes that contain the sides of the removed hexagon) to perform translation operations to obtain the desired object. The basal fault in the initial configuration is then of type BB. After that, the atomic structure is relaxed. During DFT and MS relaxation, there is a stabilization of hexagonal-based pyramids with stacking faults on first order pyramidal planes, close to $\{10\bar{1}1\}$ on the six facets and with a fault in the basal plane. However, this basal fault evolves differently in DFT and MS, as shown in Figure 3, which represents a sectional view in the plane (0001) of the pyramid. The MS relaxation calculations show that the object retains its BB basal fault whatever its size. On the contrary, in DFT, there is a progressive transition of the basal stacking fault from the type BB to the type I_1, represented by the green color atoms. In fact, these results illustrate the deficiency of the EAM potential # 3 already pointed out in [23]: it predicts that the BB stacking is an energy minimum of the γ surface whereas it is an energy maximum according to *ab initio* calculations. This explains the persistence of BB fault in MS results which are then not reliable on that occurrence.

The DFT results suggest that the pyramids, as they grow, tend to develop the same stacking fault as the one observed experimentally in the faulted ‹c›-loop, which supports the assumption that pyramids can be a precursor for these loops.

All the DFT and MS data concerning pyramids are gathered in Figures 5 and 6. Despite the aforementioned difference on the predicted basal fault, the formation energies obtained by both techniques are remarkably close to each other, which is probably fortuitous.

Contrary to perfect loops, it was possible to stabilize ‹c› faulted dislocation loops I_1 both in MS and DFT calculations with the following method: loops were built from a BB type configuration (Figure 4-a) where the upper and lower atoms bordering the loop were shifted respectively by a fault vector $\vec{f} = 1/12[20\bar{2}\bar{3}]$ and $-\vec{f}$. In the relaxed configuration of small size defects, irrespective of the modeling method (DFT or MS), the normal to the habit plane of the loop was not exactly parallel to the [0001] direction (cf. Figure 4-c). Larger size defects simulated with the EAM potential showed no disorientation of the habit plane with respect to the basal plane. It can thus be concluded that the I_1 fault is stabilized for a number of vacancies larger than 500. During the relaxation, stacking faults always appear in the pyramidal planes of type $\Pi 1$ (cf. Figure 4-c) bordering the loop. The formation energies of these objects are also gathered in Figures 5 and 6, MS values being slightly higher than the DFT ones.

Like for bipyramids in Figure 2, it was expected that MS simulations could reproduce the morphological evolution of pyramids into faulted loops at larger sizes. However, the MS results did not show any evolution of pyramids, even for n as large as 12000 (the maximum values tested in this work). This result may be a consequence of the inability of the EAM potential to correctly reproduce the transition of the BB to I1 stacking fault obtained in DFT calculations and represented in Figure 3. A fortiori, it is logical that this potential is unable to reproduce the evolution of the pyramids into faulted loops. The limited accuracy of the EAM potential justifies to resort to the alternative approach relying on mesoscopic laws.

The goal of the next section is then twofold: (i) establishing the analytical form of the mesoscopic laws for loops and (bi)pyramids and (ii) adjusting the parameters of these laws on DFT data calculated in this section. The EAM data will also be used in the next section in order to test the validity of the procedure to obtain quantitatively reliable mesoscopic laws.

IV. Mesoscopic laws

Dislocation loops

The same approach as Varvenne et al. is used to model the formation energy of large dislocation loops [23] which is derived from elasticity theory [36]. In this approach, it is supposed that loop formation energies follow a line tension model [25] given by the following expression:

$$E^f_{loop}(R) = \pi R^2\gamma + \oint_L K(\vec{t})\,\mathrm{d}l \ln\left(\frac{R}{r_c}\right) \qquad (1)$$

The first and second right-hand terms of Eq. (1) respectively correspond to the stacking fault and elastic energy contribution of the loop. $K(\vec{t})$ represents an elastic coefficient depending on the elastic constants, the Burgers vector of the loop, and the tangent direction $\vec{t}$ of an element of length dl of the loop. The coefficients γ, r_c and R respectively represent the basal stacking fault energy, the core radius and the radius of the dislocation loop.

To write this expression as a function of the number of vacancies n, it is considered that the surface of a vacancy corresponds to the atomic surface of zirconium in the basal plane S_{at} and that the loop has a circular shape. The atomic surface in the basal plane is:

$$S_{at} = \frac{a^2\sqrt{3}}{2} \qquad (2)$$

Thus, it is possible to calculate the radius R of the loop as follows:

$$\pi R^2 = nS_{at} \qquad (3)$$

$$R = a\left(\frac{\sqrt{3}}{2\pi}\right)^{\frac{1}{2}}\sqrt{n} = R_1\sqrt{n} \qquad (4)$$

With $R_1 = a\left(\frac{\sqrt{3}}{2\pi}\right)^{\frac{1}{2}}$.

Expression (1) becomes:

$$E^f_{loop}(n) = \pi R_1^2\gamma n + 2\pi f R_1 \overline{K}\sqrt{n}\ln\left(\frac{R_1\sqrt{n}}{r_c}\right) + c_0 \qquad (5)$$

Where f and $\overline{K}$ represent respectively the shape factor of the loop and the average value of $K(\vec{t})$ along the dislocation line:

$$\overline{K} = \frac{1}{2\pi}\oint_0^{2\pi} K(\vec{t})\,\mathrm{d}\theta \qquad (6)$$

A constant c_0 was added to the expression to match the atomic data in the limit of small loop size for which the concepts of perimeter and surface are not well defined [37]. To summarize, the parameters appearing in the formation energy expression of dislocation loops are the geometrical factors R_1 and f, the elastic and stacking fault energy coefficients $\overline{K}$ and γ, the core radius r_c and the constant c_0. These parameters are reported in Table 2 in which they are classified into 2 categories depending on how their values were determined: fixed parameters are calculated from geometrical considerations or taken from the literature, whereas the adjusted parameters are chosen such as expression (5) fits the DFT or EAM formation energy curves.

Table 2: fixed and adjusted parameters considered and fitting results of dislocation loops. The core radii are expressed in unit of lattice parameter a (u.l.a.).

Parameters	Dislocation loops		Faulted		Perfect	
			EAM	DFT	EAM	DFT
R_1 (Å)	Radial factor	Fixed	$a\left(\frac{\sqrt{3}}{2\pi}\right)$		$a\left(\frac{\sqrt{3}}{4\pi}\right)$	
f	Form factor	Fixed	1	1	1	1
$\overline{K}$ (eV. Å^{-1})	Elastic coefficient	Fixed	0.33	0.25	0.68	0.60
γ (mJ.m^{-2})	Basal stacking fault energy	Fixed	99 [23]	147 [23]	-	-
r_c (u.l.a.)	Core radius of loop	Adjusted	0.34	0.30	0.20	0.20
c_0 (eV)	Constant	Adjusted	-7.99	-1.95	-	-

In order to further validate the continuous modeling of the dislocation loops, we have also compared the deformation induced by the loops at the atomic scale to the expression obtained in the framework of the continuous theory of elasticity. In the case of dislocation loops, the work of Nabarro [38] has shown that the stress field of a dislocation loop is equivalent to that of a platelet whose edge corresponds to the dislocation line and whose eigenstrain is given by:

$$\varepsilon_{ij}^{0,N} = \frac{1}{2d}(b_i n_j + b_j n_i) \qquad (7)$$

Where d represents the thickness of the loop and b_i and n_i are the components of the Burgers vector and the normal to the plane of the loop.

It is possible to compare the results given by Eq. (7) with the eigenstrain deduced from atomic simulations following the method described in Appendix B for perfect and faulted loops. Such comparisons are represented in Figure 7 for perfect loops simulated by MS: whereas the Nabarro formula predicts that ε_{xx}^{0} and ε_{yy}^{0} are null and ε_{zz}^{0} is equal to -1, the MS results $\varepsilon_{ij}^{0,MD}$ converge towards these values when the size of the loop increases, which is an expected result, since the elastic theory underlying the expression of Nabarro is more suitable to describe mesoscopic objects rather than atomic ones. However, this convergence is slow and even for loops containing 5000 vacancies, there are significant discrepancies between both approaches: $\varepsilon_{xx}^{0,MD}$ and $\varepsilon_{yy}^{0,MD}$ are equal to -0.25 according to MS simulations instead of 0, as predicted by Eq. (7), and $\varepsilon_{zz}^{0,MD}$ is equal to -0.5 instead of -1. Despite these differences, there is an excellent agreement concerning the volume expansion $\sum_{i=1,3} \varepsilon_{ii}^{0}$ represented in Figure 7 in the whole range of loop sizes investigated.

The same tendencies are observed for faulted loops in Figure 8. However, the convergence of MS values to the ones predicted by Eq. (7) when n increases is more rapid than in the case of perfect loops. A closer examination of the morphology of small loops simulated by MS reveals that their habit plane is not perfectly parallel to the basal plane. By taking into account this disorientation in Eq. (7), new values of $\varepsilon_{ij}^{0,N}$ are obtained and represented in Figure 8. These values are closer to $\varepsilon_{ij}^{0,MD}$. The consistency between both approaches confirms the existence of these disorientations for small faulted loops, this disorientation decreasing with the size of the loops. These results confirm the validity of the approach of linking the results of atomic simulations to those resulting from continuous modeling.

Stacking fault pyramids and bipyramids

In order to determine the fitting law for pyramids, it is supposed that they can be treated as inclusions, even if these pyramids do not correspond to a new phase. The first step is then to determine the volume of the inclusion V_{inc} and areas of interest of this defect based on the number of vacancies n inserted in the system (cf. Appendix C). The formation energy can be decomposed into two contributions, an elastic energy E_{el} and an interfacial energy E_{int}:

$$E_{pyra}^{f}(n) = E_{el} + E_{int}$$

According to elasticity theory, the elastic energy is proportional to the volume of the inclusion V_{inc}:

$$E_{el} = V_{inc} w_e \tag{8}$$

w_e being the elastic energy density. Under some simplifying assumptions, this density can be analytically expressed as a function of the elastic constants of the system and the stress-free strain $\varepsilon_{ij}^{0,I}$ of the inclusion. In particular, if the elastic constants are homogeneous and isotropic and $\varepsilon_{ij}^{0,I}$ is a pure dilatation, a simple expression can be obtained for w_e [39]:

$$w_e = 2\,\mu \frac{(1+\nu)}{(1-\nu)} (\varepsilon^{0,I})^2 \tag{9}$$

μ and ν being respectively the shear modulus and Poisson coefficient of the system and $\varepsilon^{0,I}$ the diagonal component of $\varepsilon_{ij}^{0,I}$. In the case of pure dilatation, $\varepsilon^{0,I}$ is directly related to the volume expansion associated to the transformation:

$$\varepsilon^{0,I} = \frac{1}{3}\frac{\Delta V}{V_{inc}} \tag{10}$$

Where ΔV is the variation of the volume related to the transformation of a portion of the parent phase into the inclusion. If we suppose that the portion of the parent phase is the pyramid lying on the loop and if the inclusion is the same pyramid to which n vacancies have been withdrawn, then $\Delta V = -nV_{at}$. It follows that:

$$\varepsilon^{0,I} = -\frac{1}{3}\frac{nV_{at}}{V_{inc}} \tag{11}$$

By combining Eq. (8), (12) and (C.4), we finally obtain:

$$E_{el}(n) = \frac{1}{4}\mu \frac{(1+\nu)}{(1-\nu)} ca^2\sqrt{n} = \Omega\mu \frac{(1+\nu)}{(1-\nu)}\sqrt{n} \tag{12}$$

With $\Omega = ca^2/4$.

The interfacial energy is associated to the stacking fault energies of the basal and pyramidal planes, respectively noted γ_b and γ_p:

$$E_{int}(n) = s_p \gamma_p n + s_b \gamma_b n \tag{13}$$

In this expression, s_b and s_p are surface per atom in the basal and pyramidal planes respectively (see Appendix C).

The resulting fitting law for pyramids is then:

$$E^{f}_{pyra}(n) = \Omega^{pyra}\mu\frac{(1+\nu)}{(1-\nu)}\sqrt{n} + s_p^{pyra}\gamma_p n + s_b\gamma_b n + c_0 \qquad (14)$$

A constant c_0 is added for the same reasons as for loops.

For bipyramids, the same formation energy can be obtained, except that $\Omega^{bipyra} = ca^2/(2\sqrt{2})$ and $s_p^{bipyra} = 2\,s_p^{pyra} = a\sqrt{3a^2+4c^2}$. In the case of the bipyramid, there is no basal fault. All the parameters used in the formation energy expression of (bi)pyramids are then the geometrical factors Ω, s_p and s_b , the elastic and stacking fault energy coefficients ν, μ γ_p, γ_b and the constant c_0. They are reported in Table 3 in which the fixed and adjusted terms have the same meaning as in Table 2.

Table 3: fixed and adjusted parameters considered and fitting results for (bi)pyramids.

Parameters	Inclusion		Pyramid		Bipyramid	
			EAM	DFT	EAM	DFT
Ω (Å^3)	Volume factor	Fixed	$ca^2/4$		$ca^2/(2\sqrt{2})$	
s_p (Å^2)	Surface factor of pyramidal facets	Fixed	$\frac{a}{2}\sqrt{3a^2+4c^2}$		$a\sqrt{3a^2+4c^2}$	
s_b (Å^2)	Basal surface factor	Fixed	$\frac{\sqrt{3}}{2}a^2$		-	
ν	Poisson coefficient	Fixed	0.3		0.3	
μ (GPa)	Shear modulus	Adjusted	29.2	34.2	35.7	31.2
γ_p (mJ.m^{-2})	Pyramidal stacking fault energy	-	Adjusted 91.1	Fixed 103 [40]	Adjusted 116	Fixed 103 [40]
γ_b (mJ.m^{-2})	Basal stacking fault energy	Adjusted	182	324	-	
c_0 (eV)	Constant	Adjusted	-6.1	-5.3	-12.9	-9.7

In order to assess the relevance of the inclusion model for pyramids/bipyramids, the analytical eigenstrain given by Eq. (11) is compared to the eigenstrain deduced from atomic simulations following the method described in Appendix B in terms of volume expansion of the defects. Figures 7 and 8 show a good agreement for both pyramids and bipyramids, which validates the inclusion model to describe the elastic behaviour of these objects. In particular, the atomic simulations reveal that the deformation induced by the pyramids or bipyramids is almost isotropic ($\varepsilon^0_{xx} = \varepsilon^0_{yy} = \varepsilon^0_{zz}$), which is consistent with the assumption made in the inclusion model.

Results of the fitting procedure

Concerning the perfect loops simulated with the EAM potential, R_1, f and $\bar{K}$ are supposed to be known and only r_c is adjusted, yielding a value of 0.2 u.l.a (in unit of lattice parameter a) (see Table 2). The resulting fitting curve is represented in Figure 10-b (dotted green line). Conserving the same analytical form and values for R_1, f and r_c, a more precise mesoscopic law for perfect loops is expected by using the value of $\bar{K}$ deduced from the elastic constants of zirconium calculated in DFT ($\bar{K} = 0.6$) instead of EAM method ($\bar{K} = 0.68$). The corresponding DFT parameters and curve are respectively given in Table 2 and represented in Figure 10-b (pink dotted line). For bipyramids, the fitting curve is adjusted on a restricted set of formation energies, instead of the entire set of MS data represented by red circles in Figure 10-b. Among the different possibilities for the choice of parameters to adjust, the set $\{\mu, \gamma_p, c_0\}$ allows to obtain a fitting curve (red line in Figure 10-b) which correctly reproduces the other MS formation energies of larger bipyramids. Moreover, the adjusted value for the shear modulus is quite close to the one calculated by MS (see Table 3), which is a supplementary validation of the fitting procedure and inclusion model. Then, as a significant advantage, this fitting procedure is valid even by taking into account MS data for small sizes of bipyramids, which is well adapted to perform the same type of adjustment from DFT data (blue circles), since only small objects can be simulated in this approach. The fitting curve from DFT (blue line in Figure 10-b) has then been obtained following the same steps, except that the value of γ_p has been fixed to the energy of the stacking fault between widely spaced pyramidal planes of the first order (calculated and referred as Pyr. I-W SF2 in [40], see Table 3). The resulting DFT fitting curves show an inversion of stability between bipyramids and perfect loops for a critical number n_c of vacancies approximately equal to 9000, bipyramids being more stable than perfect loops for $n < n_c$. This value of n_c is included inside the transition zone deduced from the direct observation of the defect morphology in MS simulations (see section III). The mesoscopic laws give further insight to explain this transition, due to two antagonist effects:

(i) for the same number of vacancies n, the elastic energy of bipyramids is lower than for loops and the difference increases with n, since the elastic energy of bipyramids is proportional to $\sqrt{n}$ whereas the elastic energy of loops is proportional to $\sqrt{n}\ln(\sqrt{n})$. The elastic energy tends to promote the formation of bipyramids.

(ii) There is a stacking fault energy contribution proportional to n associated to bipyramids, but not to perfect loops, which penalizes the bipyramids.

Each contribution varies differently with n. The stacking fault contribution being proportional to n whereas the elastic contribution varies with $\sqrt{n}$ or $\sqrt{n}\ln(\sqrt{n})$, the interfacial contribution becomes dominant for larger values of n, yielding a larger formation energy for bipyramids. It then becomes energetically favorable to form not faulted perfect loops instead.

Dimensional arguments can also be used to predict the enhanced stability of bipyramids at small sizes of defects. For perfect loops, if the elastic distortions of the lattice are neglected, the atoms seeing a defective environment are in the core of the dislocation line and their number is proportional to the length of the dislocation, equal to $2\pi f R_1\sqrt{n}$. In fact, in the case of the perfect dislocation, the formation energy of the dislocation is the sum of two contributions, a core energy term and an elastic term, which may be written as:

$$E^f_{loop}(n) = 2\pi f R_1 E_{core}\sqrt{n} + 2\pi f R_1 \bar{K}\sqrt{n}\ln\left(\frac{R_1\sqrt{n}}{r_0}\right) = 2\pi f R_1 \bar{K}\sqrt{n}\ln\left(\frac{R_1\sqrt{n}}{r_c}\right) \quad (15)$$

With E_{core} the core energy of the dislocation per unit length, r_0 the 'true' core radius and $r_c = r_0\exp(-E_{core}/\bar{K})$. It means that the core energy is already included in the analytical form of equation (1), in which r_c can be considered as an effective core radius. Then, if we neglect the elastic terms, the formation energy grows as $\sqrt{n}$ for loops while it grows as n for bipyramids. Since $\sqrt{n}$ is the leading term for small n in comparison with n, the opposite being true for large values of n, bipyramids should be more stable than loops for small n, with an inversion of stability when n increases, which corresponds qualitatively to the observed behaviour. Moreover, if we only consider the elastic energy terms, we have already shown that at large n, the bipyramids should be more stable. All these arguments show that elastic effects are less significant than the other contributions but still they have to be considered properly for a quantitative assessment of the critical value of n_c for which the transition is observed.

The same fitting procedure from DFT results has been applied to faulted loops and pyramids. Concerning pyramids, the adjustment gives a satisfactory value for the shear modulus, like for bipyramids, and a value of 324 mJ.m^{-2} for the basal stacking fault (see Table 3). In fact, this value is intermediate between the BB fault and the I_1 fault (see Table D1), which is consistent with the evolution of the pyramid when the vacancy number increases: as shown in Figure 3, the initial BB basal fault progressively turns into I_1. Since the fitting law is deduced from a set of data including pyramids with both BB and I_1 faults, an average value for γ_b is then obtained. The resulting fitting curves for pyramids and faulted loops exhibit the same qualitative behaviour as for bipyramids and perfect loops: beyond a critical value of n, faulted loops become more stable than pyramids, and then a transition pyramid/faulted loops is also expected. However, the transition occurs at a lower value of n_c approximately equal to 400. The interpretation for this result is also provided by arguments (i) and (ii), except that in the case of the faulted loops, a stacking fault energy must be also taken into account. This contribution is also proportional to n, like for pyramids, but the proportionality factor for loops is lower than for pyramids ($\pi R_1^2 \gamma < s_p^{pyra} \gamma_p + s_b \gamma_b$): it means that the stacking fault contribution penalizes pyramids and the previous explanations for the bipyramid/perfect loop transition still qualitatively hold for the pyramid/faulted loop transition.

It turns out that the specific role of bipyramids in the nucleation of perfect ‹c›-loops suggested by MS simulations is also supported by the use of mesoscopic laws parameterized with DFT data. This latter approach also supports the same type of transition between pyramids and faulted ‹c›-loops.

V. Discussion

The minimum size of the experimentally observed ‹c› loops is of the order of 10 nm [11,12] and none of them has ever been observed for smaller sizes. This result suggests that the ‹c› loops do not form continuously from the aggregation of monovacancies, but they appear, beyond a critical size, by transformation of another type of configuration. The simulation work performed in this paper shows a bipyramid appeared by natural relaxation trying to simulate a perfect ‹c› dislocation loop and that bipyramids can evolve to a perfect loop beyond a critical size. This transition mechanism observed for larger sizes suggests that pyramidal defects plays the role of precursor for ‹c› loops, which explains why small ‹c› loops cannot be observed. This interpretation can be extended to the faulted loops and on the whole, pyramids and bipyramids are more stable than ‹c› loops (perfect and faulted) at small sizes regardless of the simulation method used, DFT or MS. DFT calculations gives further insight about the pyramid/faulted loop transition: for small pyramids, the basal stacking fault remains BB and then evolves to I_1. Then, the pyramidal faults progressively disappears to reach a loop configuration. These pyramids in hcp systems can be viewed as the counterparts of stacking tetrahedrons already observed in face centered cubic metals [41–43]. As described in the introduction, defect clusters experimentally identified in zirconium alloys are mainly dislocation loops with ‹a› Burgers vector. Only for high fluence, the ‹c› component dislocation loops appear. However, some experimental data may support the existence of pyramids:

- discrete planar defects on first order $\{10\bar{1}1\}$ pyramidal planes have also been observed in [5] but the author was not able at that time to clearly conclude on the exact nature of this defect ;

- in other hcp metals like Mg, irradiation damage reveals the existence of small triangular shaped loops on stacking faults [44] which may be faces of pyramids;

- the high density of small ‹a› loops already present at low doses may prevent the observation of pyramids.

Performing further experimental investigations at low doses would be interesting to reveal the existence of such pyramidal clusters.

Figure 7 shows the eigenstrain for bipyramids and perfect loops. The transition predicted by MS between these two configurations occurs for a size of approximately 5000 vacancies. Bipyramids generate a significant eigenstrain for smaller sizes with values up to -0.5 but very little eigenstrain at large sizes (n> 200 vacancies). The perfect loop formation that appears around 5000 vacancies leads to a discontinuity of the eigenstrain, the component ε_{zz}^{0} (direction ‹c›) being significantly larger and converging with n towards the value -1 predicted by the Nabarro Eq. (7) when it is assumed that the habit plane of the loop is parallel to the basal plane. In the case of ε_{xx}^{0} and ε_{yy}^{0}, there is also a discontinuity. Qualitatively, the same arguments are also valid for simple pyramids and faulted loops, as illustrated in Figure 8. As a consequence, for both transitions, there is a discontinuous evolution of the deformation nature due to this transition, from a configuration for which the lattice is deformed a little in a rather isotropic way, to a configuration for which the deformation is strong and anisotropic. Macroscopically, it induces an isotropic and small deformation of the cladding when pyramids are still predominantly present at low doses, and an anisotropic deformation of the cladding, namely a contraction in the radial direction due to its specific texture, as soon as the pyramids transform into ‹c› loops.

In order to compare the formation energies of all these objects, mesoscopic laws are proposed to extrapolate the atomic data to larger sizes of the defects. These laws allowed to support the pyramid/faulted loop transition not revealed by MS simulations but they are also required in mesoscopic models dedicated to microstructure evolution under irradiation, such as Object Kinetic Monte Carlo (OKMC) models. Indeed, this type of models uses the binding energies E_n^b of the vacancy with a cluster of size n, defined as:

$$E_n^b = E_f(n=1) - (E_f(n) - E_f(n-1) \qquad (16)$$

Where $E_f(n=1)$, $E_f(n-1)$, and $E_f(n)$ are respectively the formation energies of the isolated vacancy, the vacancy cluster of size n-1 and size n. Figure 11 shows the obtained binding energies. The values of the large-size binding energies were determined from the mesoscopic laws deduced from DFT data. In the case of small sizes, the binding energies are directly derived from the simulated DFT configurations (as long as all small sizes have been calculated). The clusters considered are then cavities for vacancies. We see that the emission capacity of the clusters are quite high but decreases with the size of the defect clusters. One possible perspective of this work would then to use these data in OKMC model in order to calculate the evolving populations of microstructural defects. Knowing the eigenstrain and density associated to each type of defect, as represented in Figures 7 and 8, it would be possible to calculate the resulting macroscopic deformation of the cladding under irradiation. In particular, it would be interesting to study if the transition pyramids/loops are correlated to the breakaway phenomenon.

VI. Conclusions

This paper proposes a new mechanism for the formation of vacancy ‹c› loops in zirconium: at low doses, vacancy clustering occurs by forming faulted pyramids but as these growth during irradiation, the pyramidal configuration evolves into ‹c› loops. This scenario is supported by several simulation results depicted in this paper:

(i) At small sizes of the defect, MS simulations systematically predict the formation of bipyramids from an initial configuration corresponding to a perfect ‹c› loop. However, as the size of the defect increases, the characterization of the defect morphology reveal a progressive transition of bipyramids to perfect loops. The same type of transition could not be reproduced by MS for the formation of faulted ‹c› loops mostly experimentally observed. This is probably due to the EAM potential used, which artificially stabilizes the BB basal fault. The same simulations performed in DFT at small sizes reveal the formation of the I_1 fault in the base of the pyramid, which is also the type of fault evidenced in ‹c› loops.

(ii) Mesoscopic laws are proposed to extrapolate the formation energies of pyramids and ‹c› loops from DFT data. According to this approach, pyramids are more stable than loops at small sizes, but beyond a critical number of vacancies, there is an inversion of stability. This conclusion is valid for the two transitions bipyramids/perfect loops and pyramids/faulted loops.

Implications of such transitions on the macroscopic deformation of cladding tubes are expected to be significant. Indeed, the calculated eigenstrains of pyramids are low and rather isotropic, whereas the eigenstrains of ‹c› loops are much higher and strongly anisotropic. In order to confirm this assumption, it would be interesting to perform fully-parameterized OKMC and rate theory simulations. In that perspective, the mesoscopic laws established in this paper as well as the eigenstrain calculated for each type of microstructural defect could be used as input parameters for such simulations.

Acknowledgments

This work is part of the EM2VM Joint laboratory Study and Modeling of the Microstructure for Ageing of Materials. Part of the work was funded by the project CRAYON P11LY from EDF.

We would like to thank Dr Emmanuel Clouet (CEA SMRP) for fruitful discussion.

Calculations have been performed on EDF R&D HPC resources and we also acknowledge PRACE for awarding us access to resource MARCONI-KNL at CINECA in Italy and Hazel Hen at HLRS in Germany (project MORPHO – MOdelling Radiation damage: characterization of elementary PHysical prOcesses – Grant No 2016153636).

Appendix A

Formation energy can be seen as the energy cost that a fluctuation must provide to the system to form the defect. In the case of a pure element, the total formation energy $E_{f,tot}^{def}$ of a defect is the difference between the reference energy E_{ref} of a perfect crystal containing N_{ref} atoms and the energy E_{syst} of a crystal containing a defect and having N_{at} atoms. The comparison of energies must be related to systems containing the same number of atoms. This is expressed by the equation below:

$$E_{f,tot}^{def} = E_{syst} - \frac{N_{at}}{N_{réf}} E_{ref} \qquad \text{A.1}$$

Appendix B

All object relaxations were performed at constant volume (DFT and EAM). In this way, it is possible to obtain the stresses σ_{ij} exerted on the simulation box. It would also have been possible to perform the same simulations, but with zero stresses, from which it would have resulted an average deformation $\bar{\varepsilon}_{ij}$ on the simulation box. We then have from [45]:

$$\bar{\varepsilon}_{ij} = S_{ijkl}\sigma_{kl} \qquad \text{B.1}$$

Where S_{ijkl} represents the compliance tensor deduced from the tensor of the elastic constants. However, this deformation is not only characteristic of the defect, but also depends on the volume of the box. This is the reason why we compute the eigenstrain ε_{ij}^{0} of the defect, obtained by the ratio between the average deformation $\bar{\varepsilon}_{ij}$ and the volume fraction w_p of the defect:

$$\varepsilon_0 = \frac{\bar{\varepsilon}_{ij}}{w_p} \qquad \text{B.2}$$

The volume fraction w_p corresponds to the ratio between the volume of the defect and the total volume of the simulation box. In homogeneous linear elasticity, it is possible to show (see Khachaturyan [46]), that the ratio of Eq. (B.2) is independent of w_p which mean that the eigenstrain characterizes the defect independently of the volume of the box.

Appendix C

Our aim is to express the volume of the inclusion in terms of the numbers of vacancies it contains. The geometry of the simple pyramid is described in Figure C1.

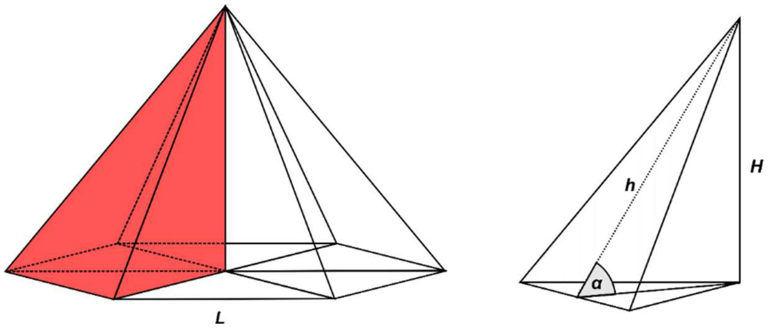

Figure C1 : Inclusion of the pyramid.

To form a faulted pyramid, a hexagonal layer containing *n* vacancies is removed from a basal atomic plane. We search to express the hexagonal surface S_b according to the number of vacancies. We consider that the atomic surface S_{at} of a vacancy and that of the removed layer S_b are related as follows:

$$nS_{at} = S_b \ with \left(\begin{array}{c} S_{at} = \dfrac{a^2\sqrt{3}}{2} \\ S_b = \dfrac{3L^2\sqrt{3}}{2} \end{array} \right) \tag{C.1}$$

It is thus easy to deduce the L side, the total volume V_{inc} of the pyramid as well as the S_p and S_b surfaces, corresponding respectively to the length of one side of the hexagon, the volume of the pyramid, the total area of the pyramidal planes and the area of the basal plane, according to the number n of vacancies.

$$\alpha = \tan^{-1}\left(\frac{2c}{a\sqrt{3}}\right) \tag{C.2}$$

$$L = \frac{a}{\sqrt{3}}\sqrt{n} \tag{C.3}$$

$$V_{inc} = 6V_{tetra} = 6\frac{B_{tetra}H}{3} = \frac{\sqrt{3}}{2}\frac{c}{a}L^3 = \frac{1}{6}a^2 c\, n^{3/2} \tag{C.4}$$

$$S_b = 6B_{tetra} = 6\frac{L^2\sqrt{3}}{4} = \frac{\sqrt{3}}{2}a^2 n \tag{C.5}$$

$$S_p = 6\frac{Lh}{2} = 3L^2\sqrt{\frac{3}{4} + \left(\frac{c}{a}\right)^2} = \frac{a}{2}\sqrt{3a^2 + 4c^2}\, n \tag{C.6}$$

V_{tetra} is the volume of one tetrahedron represented in red in figure C1 and B_{tetra} is its basal surface.

Appendix D

In hcp structure, there are different types of stacking faults in basal plane when removing one atomic layer [47].

Table D1: List of existing basal stacking fault. The column labeled “Operation” concern the colorized letters. The dot “.” between the letters sequence represent the fault emplacement.

Fault	Initial stacking	Operation	Final stacking	Burger vector	Fault energy (mJ.m^{-2})
BB	ABAB.**A**BAB	Remove the layer **A**	ABAB.BABAB	$1/2[0001]$	575 [23]
I_1	ABAB.**BABA**	Shifted by $1/3\langle 10\bar{1}0\rangle$	ABAB.CBCBC	$1/6\langle 20\bar{2}3\rangle$	160 [23,40]
I_2	ABAB.**B**A**B**A	Shifted by $1/3\langle 10\bar{1}0\rangle$	ABAB.CACAC		220 [23,40]
E	ABAB.**B**ABA	Shifted by $1/3\langle 10\bar{1}0\rangle$	ABAB.CABAB	$1/2[0001]$	280 [23,40]

Table D2: Stacking fault energy in the $(\bar{1}011)$ π_1 pyramidal plane.

Methods	Vector	γ_p (mJ.m^{-2})	Ref.
VASP PW US 10e	$0.250[10\bar{1}2]$	240^a	[48]
PWSCF PBE US 12e	$0.212[10\bar{1}2]$	127 (215^a)	[49–51]
VASP PBE 12e	-	103	[40]
EAM #3	-	243^a	[49]

^{a}Atomic relaxations only in the direction perpendicular to the fault plane

VII. Bibliographic references

[1] A. Rogerson, Irradiation growth in zirconium and its alloys, Journal of Nuclear Materials. 159 (1988) 43–61.

[2] G. Carpenter, R. Zee, A. Rogerson, Irradiation growth of zirconium single crystals: A review, Journal of Nuclear Materials. 159 (1988) 86–100.

[3] M. Griffiths, R. Gilbert, V. Fidleris, R. Tucker, R. Adamson, Neutron damage in zirconium alloys irradiated at 644 to 710 K, Journal of Nuclear Materials. 150 (1987) 159–168.

[4] F. Onimus, J. Béchade, Radiation effects in zirconium alloys, Comprehensive Nuclear Materials, Elsevier. (2012) 1–31.

[5] M. Griffiths, A review of microstructure evolution in zirconium alloys during irradiation, Journal of Nuclear Materials. 159 (1988) 190–218.

[6] A. Jostsons, R. Blake, J. Napier, P. Kelly, K. Farrell, Faulted loops in neutron-irradiated zirconium, Journal of Nuclear Materials. 68 (1977) 267–276.

[7] M. Griffiths, M. Loretto, R. Smallman, Anisotropic distribution of dislocation loops in HVEM-irradiated Zr, Philosophical Magazine A. 49 (1984) 613–624.

[8] M. Griffiths, R. Gilbert, The formation of c-component defects in zirconium alloys during neutron irradiation, Journal of Nuclear Materials. 150 (1987) 169–181.

[9] D. Northwood, R. Gilbert, L. Bahen, P. Kelly, R. Blake, A. Jostsons, P. Madden, D. Faulkner, W. Bell, R. Adamson, Characterization of neutron irradiation damage in zirconium alloys—an international “round-robin” experiment, Journal of Nuclear Materials. 79 (1979) 379–394.

[10] L. Tournadre, F. Onimus, J.-L. Béchade, D. Gilbon, J.-M. Cloué, J.-P. Mardon, X. Feaugas, O. Toader, C. Bachelet, Experimental study of the nucleation and growth of c-component loops under charged particle irradiations of recrystallized Zircaloy-4, Journal of Nuclear Materials. 425 (2012) 76–82.

[11] N. Gharbi, F. Onimus, D. Gilbon, J.-P. Mardon, X. Feaugas, Impact of an applied stress on c-component loops under Zr ion irradiation in recrystallized Zircaloy-4 and M5®, Journal of Nuclear Materials. 467 (2015) 785–801.

[12] N. Gharbi, Contribution to the understanding of zirconium alloy deformation under irradiation at high doses, Thèse, Université de La Rochelle, 2015.

[13] M. Gaumé, F. Onimus, L. Dupuy, O. Tissot, C. Bachelet, F. Mompiou, Microstructure evolution of recrystallized Zircaloy-4 under charged particles irradiation, Journal of Nuclear Materials. 495 (2017) 516–528.

[14] R. Holt, R. Gilbert, c-Component dislocations in neutron irradiated zircaloy-2, Journal of Nuclear Materials. 116 (1983) 127–130.

[15] R. Holt, R. Gilbert, < c> Component dislocations in annealed Zircaloy irradiated at about 570 K, Journal of Nuclear Materials. 137 (1986) 185–189.

[16] R. Holt, Mechanisms of irradiation growth of alpha-zirconium alloys, Journal of Nuclear Materials. 159 (1988) 310–338.

[17] R. Gilbert, K. Farrell, C. Coleman, Damage structure in zirconium alloys neutron irradiated at 573 to 923 k, Journal of Nuclear Materials. 84 (1979) 137–148.

[18] F. Christien, A. Barbu, Cluster Dynamics modelling of irradiation growth of zirconium single crystals, Journal of Nuclear Materials. (2009) 153–161.

[19] A. Barashev, S. Golubov, R. Stoller, Theoretical investigation of microstructure evolution and deformation of zirconium under neutron irradiation, Journal of Nuclear Materials. (2015) 85–94.

[20] C. Woo, Theory of irradiation deformation in non-cubic metals: effects of anisotropic diffusion, Journal of Nuclear Materials. 159 (1988) 237–256.

[21] Y. de Carlan, C. Regnard, M. Griffiths, D. Gilbon, C. Lemaignan, Influence of Iron in the Nucleation of< c> Component Dislocation Loops in Irradiated Zircaloy-4, in: Zirconium in the Nuclear Industry: Eleventh International Symposium, ASTM International, 1996.

[22] D. Kulikov, M. Hou, Vacancy dislocation loops in zirconium and their interaction with self-interstitial atoms, Journal of Nuclear Materials. 342 (2005) 131–140.

[23] C. Varvenne, O. Mackain, E. Clouet, Vacancy clustering in zirconium: An atomic-scale study, Acta Materialia. 78 (2014) 65–77.

[24] M.I. Mendelev, G.J. Ackland, Development of an interatomic potential for the simulation of phase transformations in zirconium, Philosophical Magazine Letters. 87 (2007) 349–359.

[25] D. Bacon, D. Barnett, R.O. Scattergood, Anisotropic continuum theory of lattice defects, Progress in Materials Science. 23 (1980) 51–262.

[26] R. Voskoboinikov, Y.N. Osetsky, D. Bacon, Identification and morphology of point defect clusters created in displacement cascades in α-zirconium, Nuclear Instruments and Methods in Physics Research Section B: Beam Interactions with Materials and Atoms. 242 (2006) 530–533.

[27] G. Ackland, S. Wooding, D. Bacon, Defect, surface and displacement-threshold properties of α-zirconium simulated with a many-body potential, Philosophical Magazine A. 71 (1995) 553–565.

[28] S. Di, Molecular Dynamics Simulation of Irradiation Damage in α-Zirconium, PhD Thesis, Thesis, Queen’s University, 2016.

[29] G. Kresse, J. Furthmüller, Software VASP, vienna (1999), Phys. Rev. B. 54 (1996) 169.

[30] J.P. Perdew, Y. Wang, Accurate and simple analytic representation of the electron-gas correlation energy, Physical Review B. 45 (1992) 13244.

[31] P.E. Blöchl, Projector augmented-wave method, Physical Review B. 50 (1994) 17953.

[32] M. Methfessel, A. Paxton, High-precision sampling for Brillouin-zone integration in metals, Physical Review B. 40 (1989) 3616.

[33] C. Varvenne, F. Bruneval, M.-C. Marinica, E. Clouet, Point defect modeling in materials: coupling ab initio and elasticity approaches, Physical Review B. 88 (2013) 134102.

[34] S. Plimpton, Fast parallel algorithms for short-range molecular dynamics, Journal of Computational Physics. 117 (1995) 1–19.

[35] A. Khachaturyan, Theory of structural phase transformations in solids, John Willey, New York, NY. 17 (1983) 1733–1743.

[36] J.H.J. Lothe, J.P. Hirth, Theory of dislocations, Wiley, New York. (1982) 270.

[37] R. Alexander, M.-C. Marinica, L. Proville, F. Willaime, K. Arakawa, M. Gilbert, S. Dudarev, Ab initio scaling laws for the formation energy of nanosized interstitial defect clusters in iron, tungsten, and vanadium, Physical Review B. 94 (2016) 024103.

[38] F. Nabarro, CXXII. The synthesis of elastic dislocation fields, The London, Edinburgh, and Dublin Philosophical Magazine and Journal of Science. 42 (1951) 1224–1231.

[39] J.D. Eshelby, The determination of the elastic field of an ellipsoidal inclusion, and related problems, Proceedings of the Royal Society of London. A241 (1957) 376–396.

[40] B. Yin, Z. Wu, W. Curtin, Comprehensive first-principles study of stable stacking faults in hcp metals, Acta Materialia. 123 (2017) 223–234.

[41] J. Silcox, P. Hirsch, Direct observations of defects in quenched gold, Philosophical Magazine. 4 (1959) 72–89.

[42] J. Edington, R. Smallman, Faulted dislocation loops in quenched aluminium, Philosophical Magazine. 11 (1965) 1109–1123.

[43] L. Zhang, C. Lu, G. Michal, G. Deng, K. Tieu, The formation and destruction of stacking fault tetrahedron in fcc metals: A molecular dynamics study, Scripta Materialia. 136 (2017) 78–82.

[44] M. Griffiths, Evolution of microstructure in hcp metals during irradiation, Journal of Nuclear Materials. 205 (1993) 225–241.

[45] E. Clouet, S. Garruchet, H. Nguyen, M. Perez, C.S. Becquart, Dislocation interaction with C in α-Fe: A comparison between atomic simulations and elasticity theory, Acta Materialia. 56 (2008) 3450–3460.

[46] A. Khachaturyan, Theory of structural phase transformations in solids, John Willey, New York, NY. 17 (1983) 1733–1743.

[47] A. Berghezan, E.B. Simonsen, Horizontal induction zone melting of refractory metals and semiconductor materials, TRANSACTIONS OF THE METALLURGICAL SOCIETY OF AIME. 221 (1961) 1029–1031.
[48] C. Domain, Simulations atomiques ab initio des effets de l'hydrogene et de l'iode dans le zirconium, Thèse, Université de Lille 1, 2002.
[49] N. Chaari, Modélisation ab initio de la plasticité dans les métaux hexagonaux purs, zirconium et titane, et effet de l'oxygène, Thèse, Université Grenoble Alpes, 2015.
[50] N. Chaari, E. Clouet, D. Rodney, First Order Pyramidal Slip of 1/3 <1-210> Screw Dislocations in Zirconium, Metallurgical and Materials Transactions A. 45 (2014) 5898–5905.
[51] W. Szewc, L. Pizzagalli, S. Brochard, E. Clouet, Onset of plasticity in zirconium in relation with hydrides precipitation, Acta Materialia. 114 (2016) 126–135.

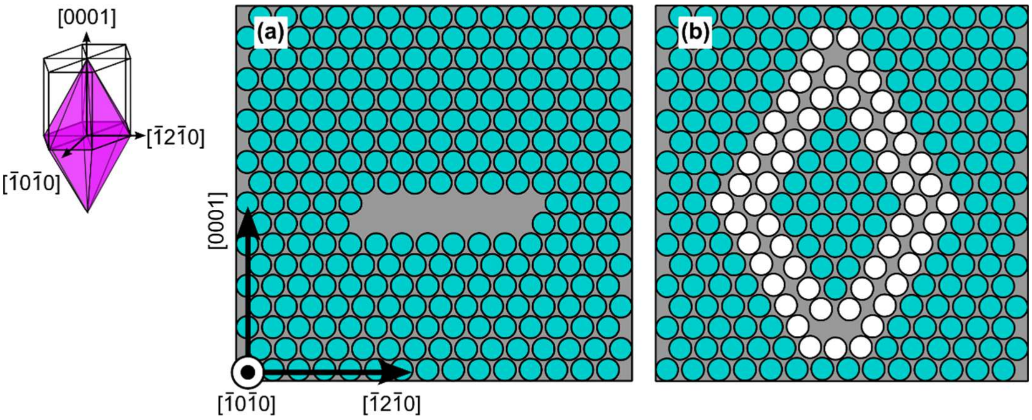

Figure 1: Construction scheme of a stacking fault bipyramid containing 96 vacancies. (a) Initial and (b) relaxed configuration obtained by the DFT method. A stacking fault is present between white atoms.

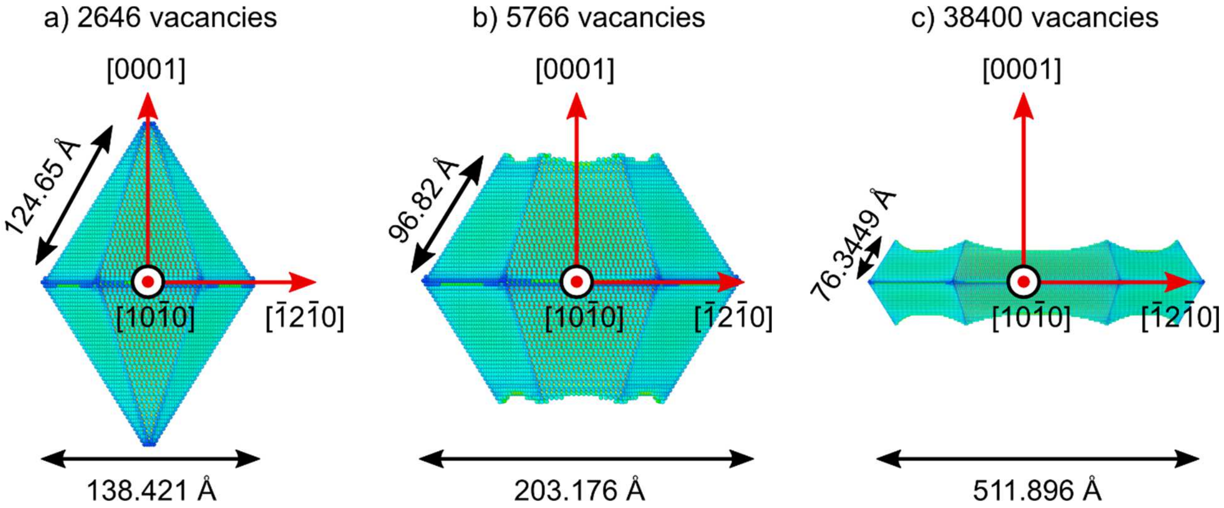
a) 2646 vacancies

b) 5766 vacancies

c) 38400 vacancies

Figure 2: Transition from bipyramid to ‹c› loop. The visualization of the defect was obtained by filtering the volumes of Voronoï where those corresponding to the perfect crystal were removed. The number of vacancies of each defect is indicated.

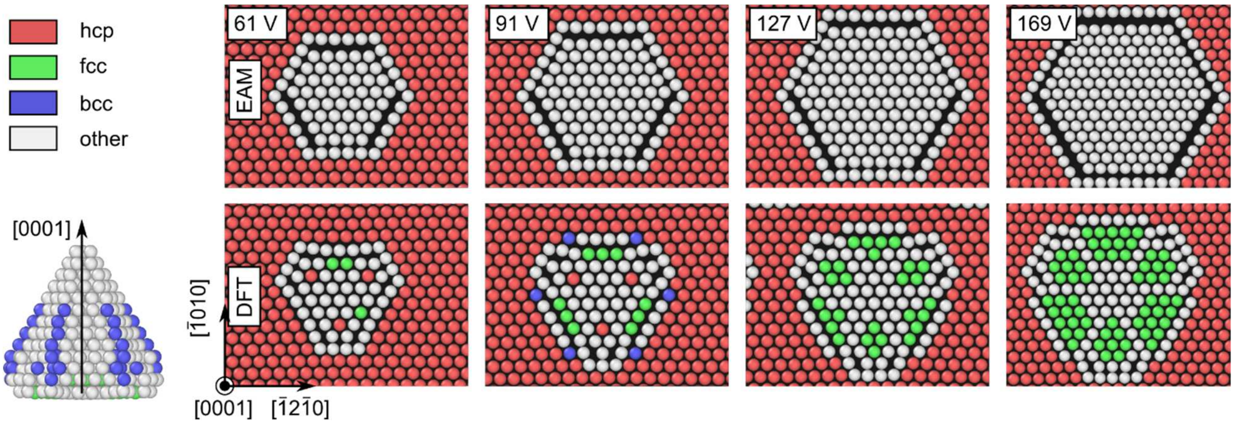

Figure 3: Evolution of stacking fault pyramid for DFT and EAM methods. The atoms are colored according to their local environment.

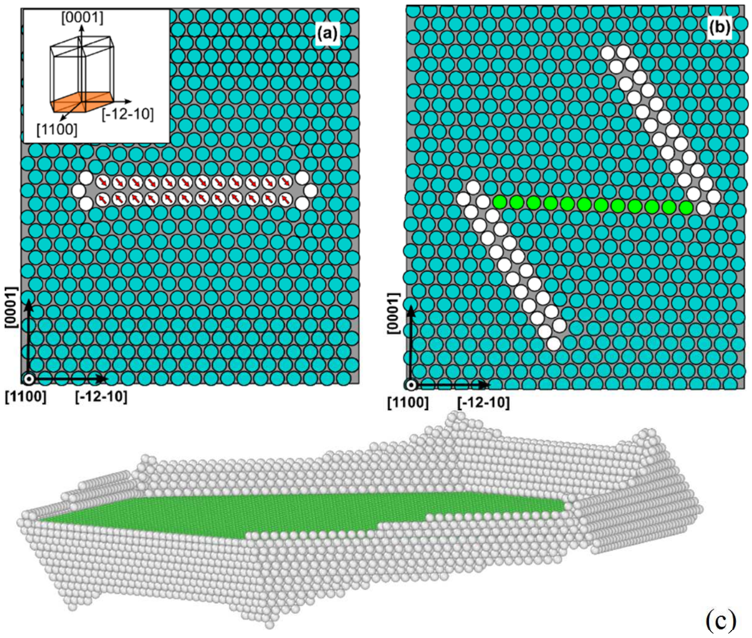

Figure 4: Construction scheme of a ‹c› dislocation loop I_1 containing 169 vacancies. (a) Initial and (b) relaxed configuration obtained with the EAM potential # 3. (c) 3D view of the final defect.

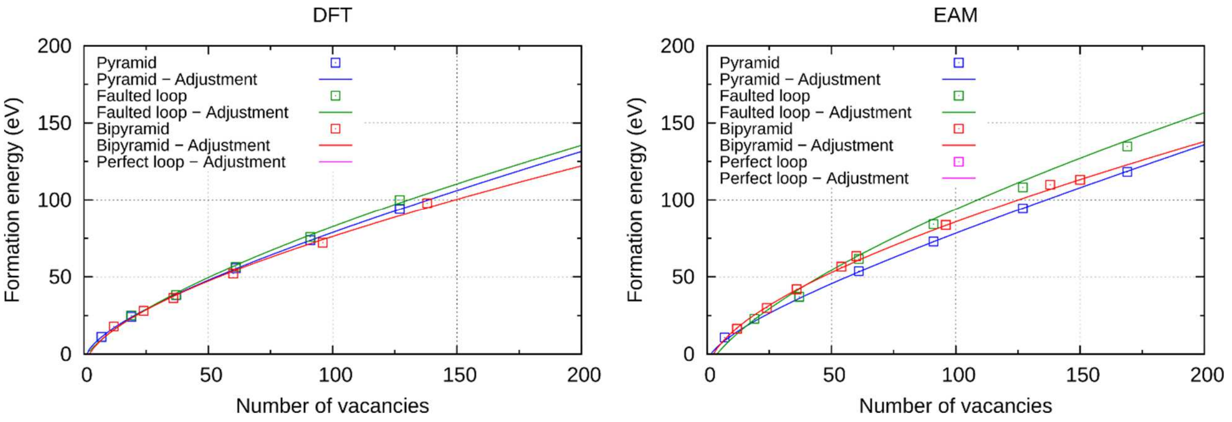

Figure 5: Formation energies of (bi) pyramids and loops as a function of the number of vacancies of the defect.

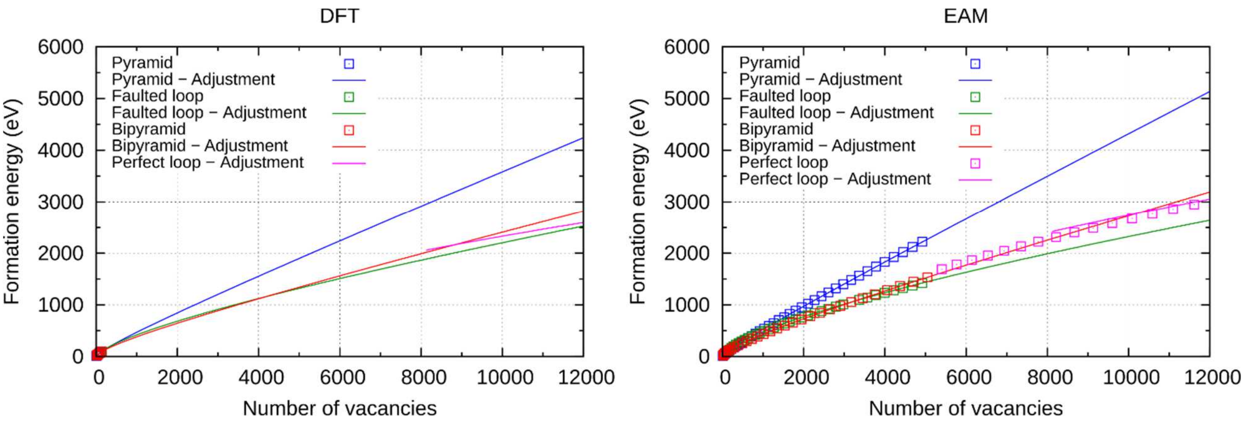

Figure 6: Formation energies of (bi) pyramids and loops as a function of the number of vacancies of the defect. This is an extrapolation of the previous figure towards a higher vacancies number.

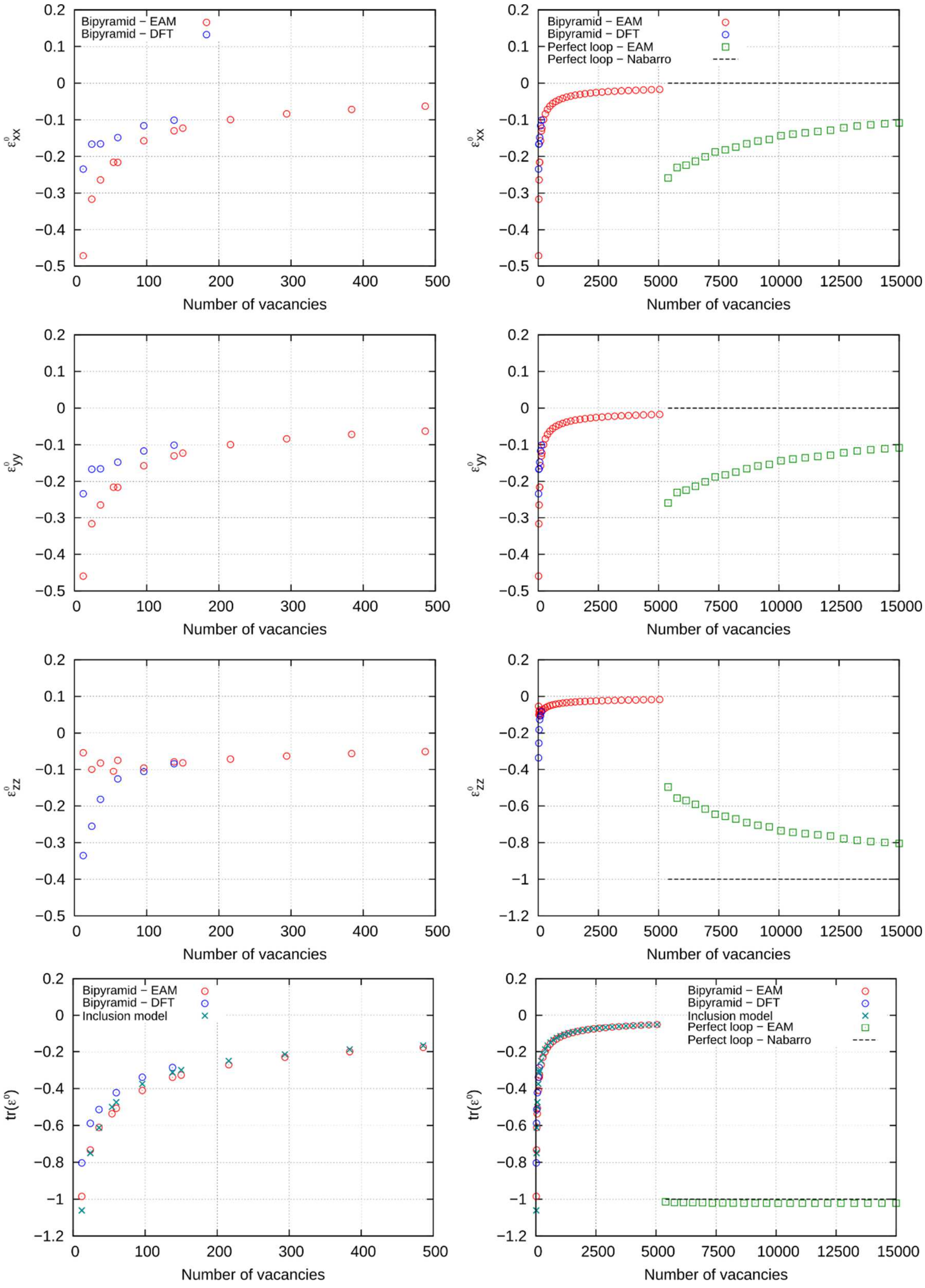
Bipyramid − EAM
Bipyramid − DFT
Perfect loop − EAM
Perfect loop − Nabarro
Inclusion model
ε^0_{xx}
ε^0_{yy}
ε^0_{zz}
$\mathrm{tr}(\varepsilon^0)$
Number of vacancies
0
100
200
300
400
500
2500
5000
7500
10000
12500
15000
0.2
0.1
0
−0.1
−0.2
−0.3
−0.4
−0.5
−0.6
−0.8
−1
−1.2

Figure 7: Eigenstrain component for bipyramids and ‹c› perfect loops as a function of the number of vacancies of the defect. The eigenstrain labeled “Nabarro” is calculated with equation (7) by considering that the habit plane of the loop is the basal plane.

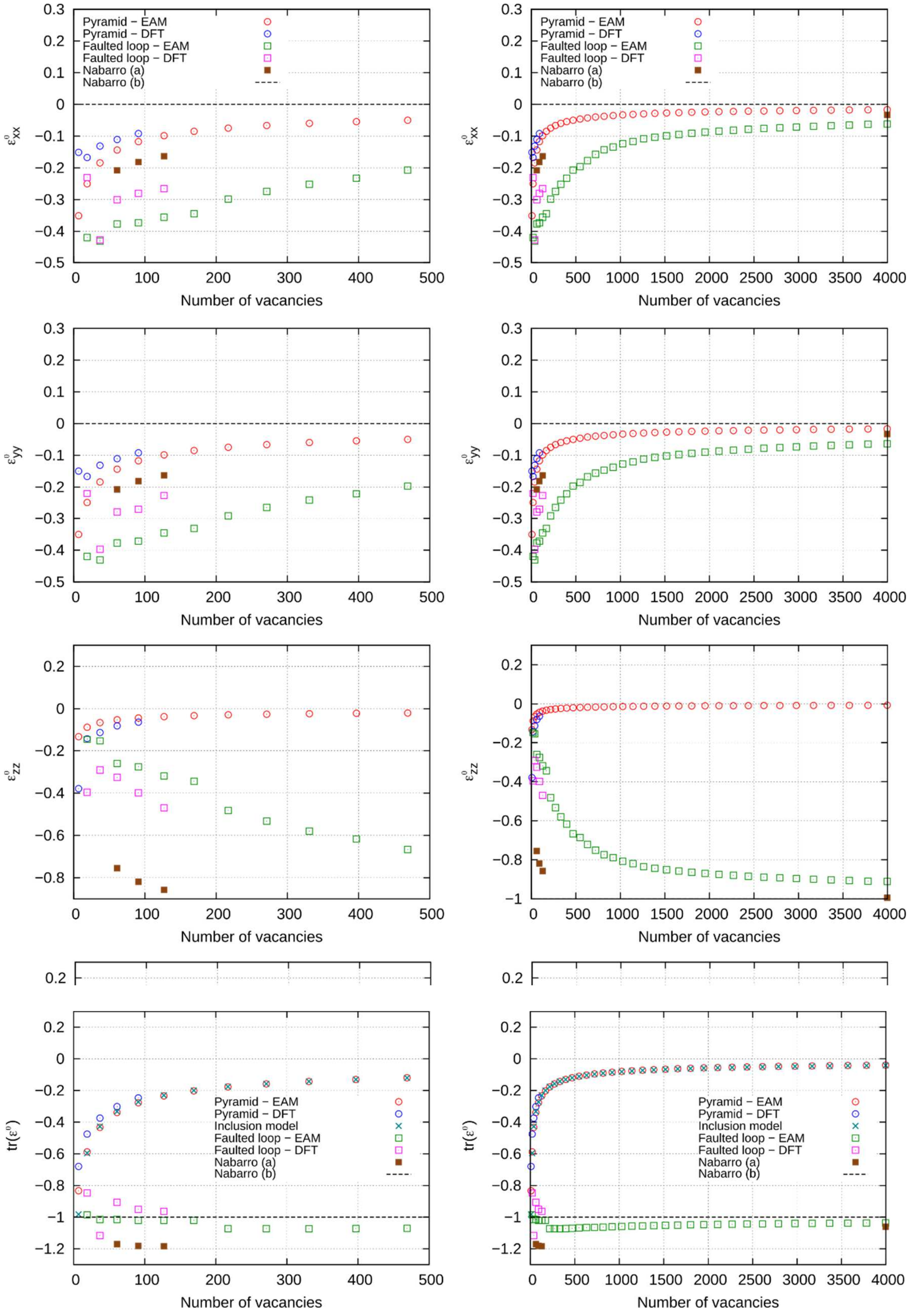
Pyramid − EAM
Pyramid − DFT
Faulted loop − EAM
Faulted loop − DFT
Nabarro (a)
Nabarro (b)
Inclusion model
ε^0_{xx}
ε^0_{yy}
ε^0_{zz}
$\mathrm{tr}(\varepsilon^0)$
Number of vacancies
0.3
0.2
0.1
0
−0.1
−0.2
−0.3
−0.4
−0.5
−0.6
−0.8
−1
−1.2
0
100
200
300
400
500
1000
1500
2000
2500
3000
3500
4000

Figure 8: Eigenstrain component for pyramids and ‹c› faulted loops as a function of the number of vacancies of the defect. The eigenstrain labeled “Nabarro” is calculated with equation (7) by considering that the habit plane of the loop is the one determined from atomistic calculations (a) or the basal plane (b).

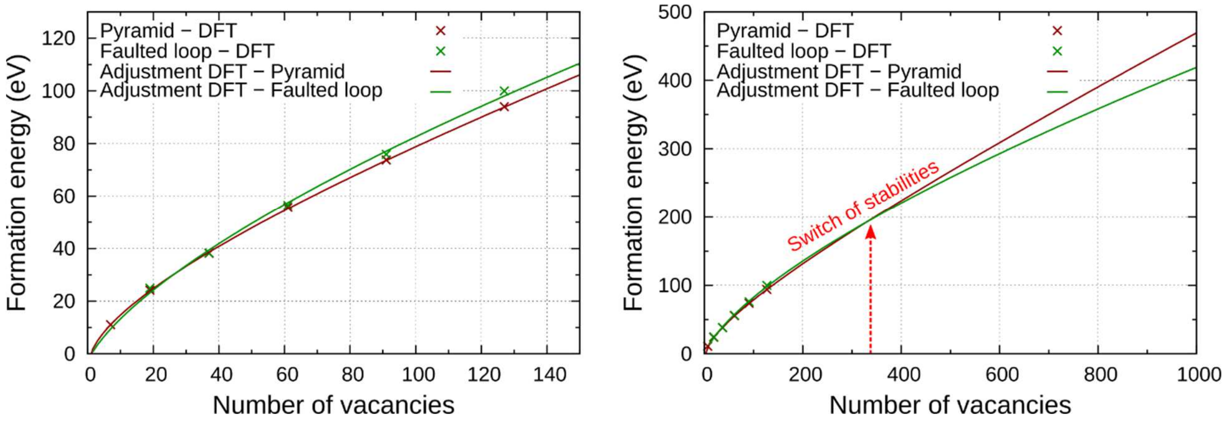

Figure 9: Difference of stability between pyramids and ‹c› faulted loops as a function of the number of vacancies of the defect.

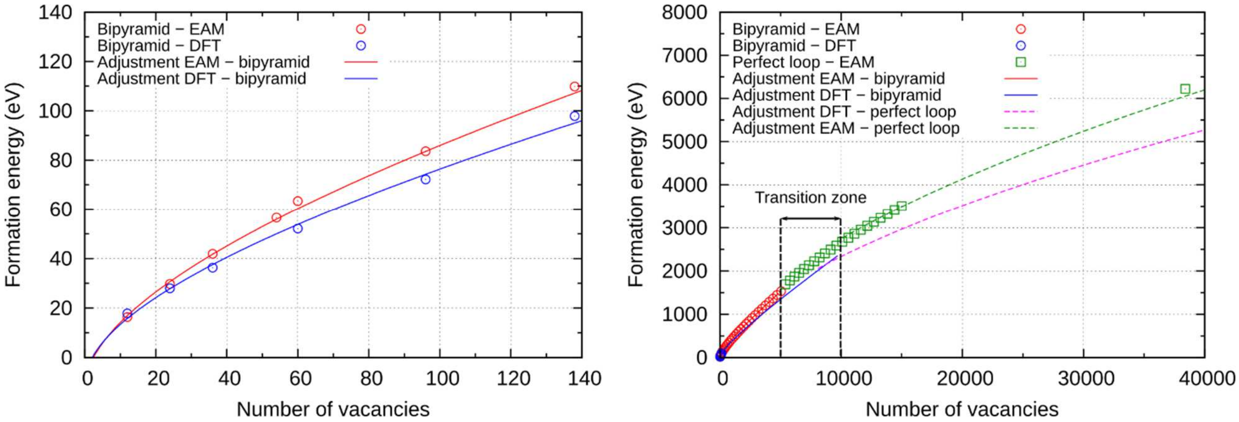

Figure 10: Difference of stability between bipyramids and ‹c› perfect loops as a function of the number of vacancies of the defect.

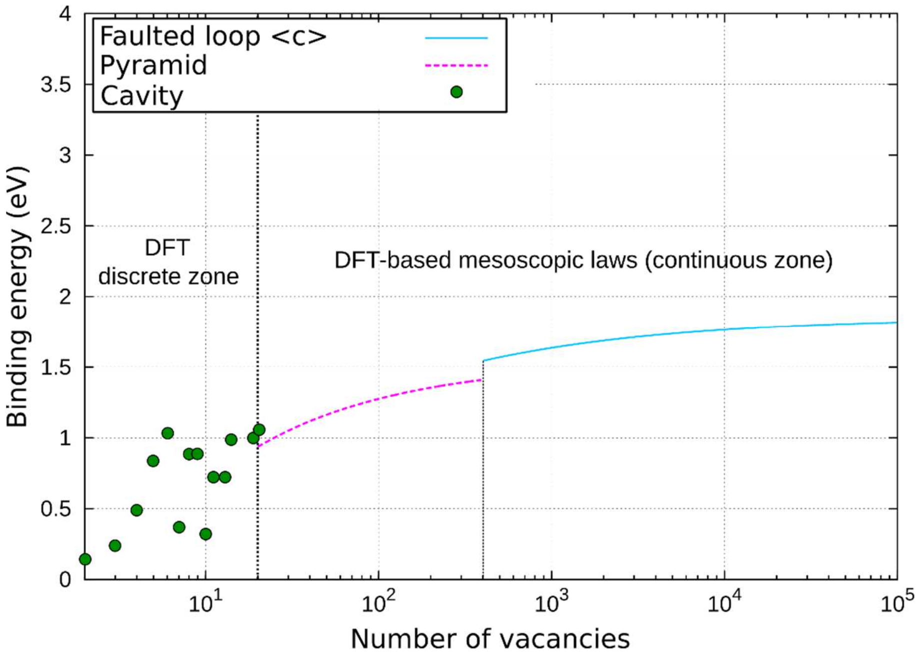

Figure 11: Binding energy of the vacancy to the different clusters as a function of the number of vacancies.

Atomic Scale modeling

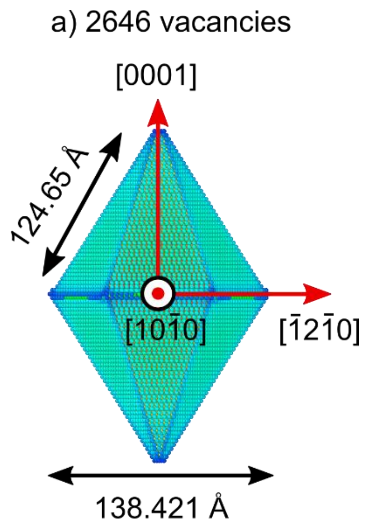

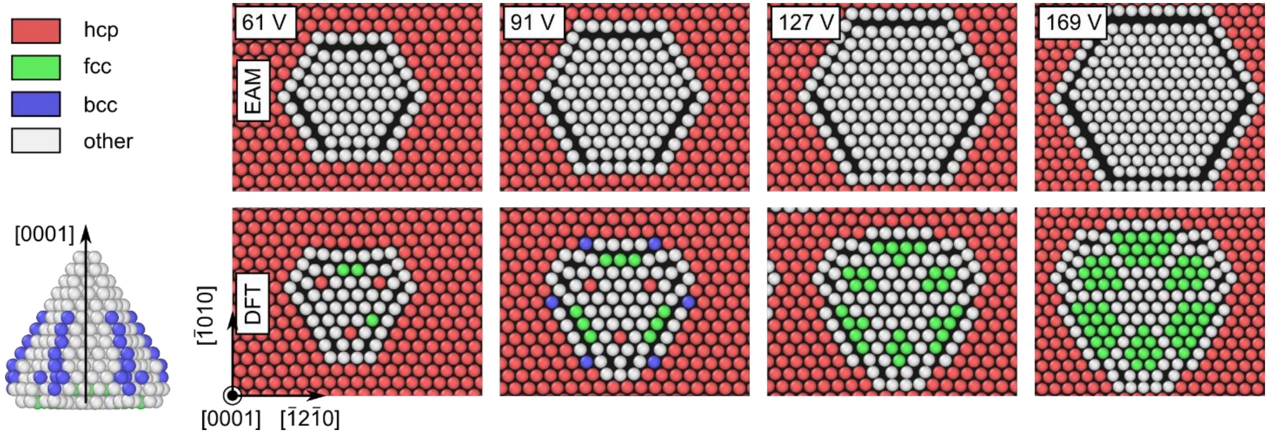

Mesoscopic model

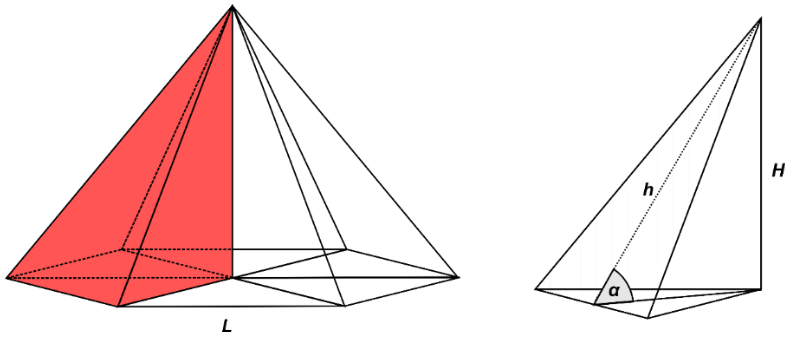

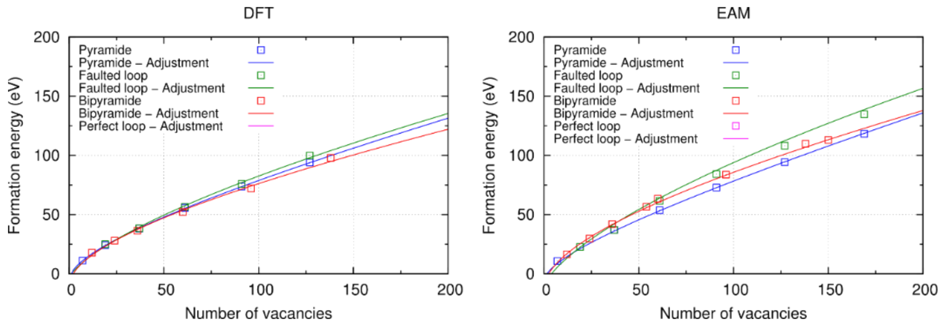

A new scenario for ‹c› vacancy loop formation in zirconium